Spatially distributed porosity: A laser powder bed fusion strategy to enhance plasticity in Zr-based metallic glass without yield stress drop

Materials & Design 260 (2025) 115145

Contents lists available at ScienceDirect

Materials & Design

journal homepage: www.elsevier.com/locate/matdes

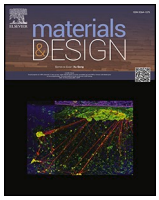

Spatially distributed porosity: A laser powder bed fusion strategy to enhance plasticity in Zr-based metallic glass without yield stress drop

Camille Pauzon [a,b,*], Rémi Daudin [a], Muhammad Fakhry Hatta [a], Pierre Lhuissier [a], Jean-Jacques Blandin [a]

[a] Université de Grenoble Alpes, CNRS, Grenoble INP, Laboratoire SIMaP, Grenoble, France
[b] Chalmers University of Technology, Division of Materials and Manufacture, Gothenburg, Sweden

ARTICLE INFO

Keywords:
Bulk metallic glasses
Laser powder bed fusion
Porosity spatial distribution
Plasticity
Hatch spacing

ABSTRACT

Laser powder bed fusion (LPBF) is a promising method to produce large metallic glass parts with complex geometry. Although Zr-based metallic glasses have a relatively good LPBF processability, they currently in most cases suffer from a lack of plastic deformation in compression compared to samples produced by conventional casting. This study demonstrates that introducing a favourable pore population with spatially controlled organisation can improve the plasticity without adversely affecting the yield stress. Taking advantage of the design freedom of the laser strategy, not only the volume fraction of pores but also their spatial distribution can be controlled by adjusting the hatch spacing distance. Combining X-ray microtomography, compression testing and scanning electron microscopy characterization reveals the enhanced interactions of shear bands with pores. This is promising for the production of strong and ductile metallic glass components using additive manufacturing.

1. Introduction

The lack of long-range order in the atomic structure of metallic glasses (MGs) endows them with exceptional properties when compared to their crystalline counterparts. MGs exhibit very high elastic limit and hardness combined with particularly large elastic strain and possibly high toughness and corrosion resistance. However, the need to maintain sufficiently high cooling rates to avoid crystallisation results in significant geometric limitations in casting processes, which greatly reduces their industrial use. Additive manufacturing (AM) and in particular laser powder bed fusion (LPBF) appears as an interesting way of overcoming these geometric constraints in the case of MGs.

In recent years, numerous studies have demonstrated the feasibility of producing metallic glasses using LPBF [1–5]. Amorphous and nearly fully dense structures have been successfully produced, particularly in the case of the AMZ4 grade ($Zr_{59.3}Cu_{28.8}Al_{10.4}Nb_{1.5}$, at.%), but the deformability of metallic glasses produced by AM [1–3] is generally lower than that of glasses produced by casting processes [2,4]. This reduced plastic strain of additively manufactured MGs is regularly attributed to a higher oxygen content, the residual presence of lack of fusion flaws, partial crystallization or a more relaxed state of the glass structure [5–8]. Therefore, overcoming the brittleness of LPBF-produced metallic glass to unlock their structural potential remains an unsolved challenge in the field. Because of this limitation, plasticity has mostly been investigated with compression and bending tests. In case of $Zr_{59.3}Cu_{28.8}Al_{10.4}Nb_{1.5}$, the few studies with tensile testing report no visible plasticity [9,10], which underlines the severity of the challenge.

It has been previously shown that the presence of pores could promote the multiplication of shear bands and therefore be an interesting way for increasing the plasticity of metallic glasses. For example, fine dispersion of pores was introduced by high-pressure hydrogenation treatment in the case of Pd-based metallic glasses to reach porosity content of 2 %–4 %, which in turn enhanced the compressive plastic strain but at the expense of a relative decrease of the yield stress [11]. Combination of experimental and modelling work on the interactions between pores, homogeneously distributed in 2D by thermoplastic forming, and shear bands has shown that the spatial distribution of pores could also be a key factor in promoting tensile ductility [12]. However, few approaches have demonstrated three-dimensional control and scalability, which are needed for various applications.

In the field of MGs processed by LPBF, a recent work by Zhang et al. [13] has confirmed the positive effect of porosity on the ductility of MGs processed by LPBF. The authors produced samples with porosity contents up to 17 % and showed that ductility could increase with

* Corresponding author.
E-mail address: pauzon@chalmers.se (C. Pauzon).

https://doi.org/10.1016/j.matdes.2025.115145
Received 1 October 2025; Received in revised form 10 November 2025; Accepted 12 November 2025
Available online 14 November 2025

increasing porosity. Their printed samples exhibited serrated plastic flow, and the porous samples had smaller stress drop magnitudes than their dense counterparts. Using FEM modelling, they observed that multiple shear bands could form in the porous sample along different directions, whereas denser samples only formed a single major shear band. However, due to the relatively high porosity content needed to obtain a significant effect on deformability, the increase in ductility was accompanied by an important decrease in yield stress.

The numerical work of Zhang et al. [14] confirmed the importance of the spatial distribution of pores and showed that different amount (4 % and 10 %) and different patterns of pores can lead to various nucleation and propagation mechanism of shear bands leading to distinct effectiveness on the plastic response. Most investigations into the beneficial effects of pores have focused on as-cast glasses, which are expected to have a notably different thermal history and structural state to AM-produced samples. Therefore, it would be beneficial for the community to explore whether pores should be considered as more than mere defects via the AM route too.

Apart from the contribution from Zhang et al. [13] and the discussion provided by Deng et al. in [2], porosity, and in particular lack of fusion pores, is considered a hazardous threat to the mechanical performance of metallic glasses produced by LPBF. Published work around LPBF of BMGs mainly focuses on maximizing density while maintaining a defect-free, amorphous material [4,10,15,16]. The present work represents a paradigm shift by intentionally harnessing, rather than eliminating, pores to enhance the mechanical response. By strategically optimizing the laser processing parameter, we demonstrate that AM can uniquely control both the amount and the spatial distribution of the pores, in ways hardly achievable through conventional manufacturing. This approach potentially offers the possibility to limit the total porosity content to preserve the yield stress, while also ensuring an appropriate spatial distribution of the pores to promote a significant beneficial effect on plasticity.

The aim of this paper is to propose such a strategy for increasing the plastic deformation capacity of a Zr-based metallic glass produced by LPBF. This is critical to be able to fully realise the design freedom promised with AM and develop amorphous structural applications, with possibly complex shapes. In the present paper, the population of pores is managed thanks to a change in hatch spacing, which has been identified as a critical parameter for controlling density in additively manufactured conventional crystalline alloys as it affects the pore nucleation, growth and outgassing [17]. Herein, the compressive behaviour of the metallic glass is evaluated and connected to its pore population, as determined by X-ray microtomography and scanning electron microscopy. Statistical analysis of the compression curves, alongside observation of interrupted mechanical tests, provide new insight into the pore-shear band interaction taking place in porous LPBF BMGs. This work paves the way for the design of strong and ductile glass heterostructure using the laser strategy as a design tool.

2. Materials and methods

Laser powder bed fusion was performed to produce MG specimens using a virgin powder feedstock of $Zr_{59.3}Cu_{28.8}Al_{10.4}Nb_{1.5}$ in at.% (Amloy-Zr01, formerly known under the trade name AMZ4, supplied by Hereaus). The particle size distribution of the powder is in the range of 15 μm to 45 μm, and its composition is given in Table 1, the alloying elements being measured by inductively coupled plasma-optical emission spectrometry (ICP-OES) and the impurities by combustion gas analysis.

An EOS M290 machine (EOS GmbH) equipped with a Yb fibre laser of 400 W nominal maximum power was employed. Parallelepiped samples with dimensions of 6 × 6 × 7.4 mm^3 were produced. A first batch of samples (called H100 in the following) were manufactured with the following parameters: laser power $\mathbf{P} = 70$ W, scanning speed $\mathbf{v} = 2000$ mm/s, layer thickness $\mathbf{t} = 20$ μm and hatch spacing $\mathbf{h} = 100$ μm, leading to a volumetric energy $E_V = \frac{P}{v\,h\,t} \approx 18$ J/mm^3. For each layer, all samples were scanned a first time and a second time thereafter, with the second laser scan identical to the first one. The bidirectional scan pattern was rotated by 67° increments between layers and at the end of the 5 h build job, the samples were removed from the Ti Grade 5 baseplate. In order to produce a spatially controlled population of porosities, a second batch of samples (called H150 in the following) was elaborated with the hatch spacing increased up to 150 μm, the other parameters being adjusted to maintain constant the volumetric energy, *i.e.* of about 18 J/mm^3.

The amorphous nature of the samples was verified by laboratory X-ray diffraction (XRD) with a PANalytical X'Pert PRO MPD equipped with a Cu source (1.5041 Å). The angular range 10°–90° was scanned with a 0.05° step size and a 300 s scan step time. Samples of 50 mg were extracted from the bulk of the cubic specimens and analysed by differential scanning calorimetry (DSC) using a Mettler Toledo DSC STARe system. Graphite crucibles were used under nitrogen atmosphere. To study the relaxation, glass transition and crystallisation, a heating rate of 20 K/min was used. The glass transition and crystallisation temperature are measured at the onsets of the transformations. The oxygen content of selected specimens was determined by combustion gas analysis using a LECO O736 device.

Uniaxial compression testing at room temperature of the LPBF rod samples, 4.5 mm in height and 3 mm in diameter machined by electro discharge machining, was performed with a MTS 4/M machine with a 20 kN load cell. An acquisition frequency of 1 kHz was used. The tests were performed under a constant strain rate of 10^{-4} s^{-1}. Machine compliance was corrected for the stress–strain curve analysis taking a Young's modulus of 87 GPa as provided in the manufacturer's material datasheet and assuming that the very low porosity content (below 1 %) does not affect this value. Fracture surfaces were characterised by scanning electron microscopy (SEM) with a Zeiss Gemini SEM 500 FEG. Such compression tests are the first step in understanding the plastic deformation of the produced glasses, and will be followed by tensile tests in future work. Vickers micro-hardness was also measured with an applied load of 1 kgf (HV1). Each indent size was measured by optical microscopy and average values of 15 measurements were reported.

Laboratory X-ray computed tomography (XCT) using an EasyTom Nano-XL system from RX Solutions was conducted to obtain 3D information of the pore population with a pixel size of 5 μm. The volumes studied were 20 mm^3. The reconstructed volumes were segmented and analysed with ImageJ [18] and the Analysis3D plugin [19]. Python was used to run more advanced analysis such as nearest neighbour pore distances and orientations. The surface voxels of each pore were extracted, the closest neighbouring pores from surface-to-surface distances were identified and the angles between the connection vectors and the loading Z-axis, which is also the building direction (BD), were computed. The surface voxel extraction was performed using an erosion operation of the segmented pores. To efficiently find the nearest neighbours, a K-D tree [20] was built for the surface of each pore.

Table 1
Composition of the virgin feedstock powder.

Element	Zr	Cu	Al	Nb	C	O	H	N
	(wt.%)	(wt.%)	(wt.%)	(wt.%)	(ppm)	(ppm)	(ppm)	(ppm)
Amount	Bal.	23.6	3.5	1.88	182	650	27	17

Finally, the angles between connection vectors and the Z-axis were calculated using the dot products of these normalised vectors and the Z-axis vector.

3. Results

3.1. Structural characterisation

Fig. 1 a) displays typical diffraction patterns for both the H100 and H150 samples. No diffraction peaks are observed, confirming the amorphous nature of the samples. Similar results were obtained on all the produced samples, as presented in the supplementary material. Fig. 1 b) shows the associated DSC curves. Characteristic thermal properties, as well as oxygen contents, porosity levels measured by XCT and hardness are listed in Table 2.

The H100 and H150 samples exhibit similar values for the glass transition temperature T_g, the crystallisation temperatures T_{x0} and T_p or $\Delta T = T_{x0} - T_g$. These temperatures are also in good agreement with the literature [5,8] and the materials datasheet provided by the powder manufacturer. In addition, the similarity of the DSC curves near the glass transition and the measured relaxation enthalpy suggests no significant differences in relaxation state among the printed specimens. The two printed samples exhibit also similar oxygen contents, around 1000 ppm. One can note that this means that a significant impurity pick-up occurred during printing, since the virgin powder has only 600 ppm O_2. Such oxygen pick-up has been already reported for alloys containing elements with a high affinity for oxygen [21,22]. The increase in oxygen content is attributed to the residual oxygen in the process chamber and the high temperatures associated with laser melting of the powder bed, which has a large specific surface area.

Finally, the material produced with the larger hatch spacing has the highest porosity level (0.75 %), which remains low to preserve the mechanical resistance and confirming the ability to modify the porosity content by adjusting the hatch spacing [23].

3.2. Mechanical behaviour

Table 2 also displays hardness measurements and values of about 470–475 HV1 are measured, suggesting no significant impact of the value of the hatch distance. These results are confirmed by the stress–strain curves in compression shown in Fig. 2. The yield stresses of both the H100 and H150 samples are around 1600 MPa. This means that the increase in porosity level from 0.09 % to 0.75 % does not reduce the compressive strength. Conversely, it affects drastically the plastic strain. The H100 sample shows very limited plastic strain, which is typical of what is frequently reported for additively manufactured Zr-based metallic glasses [2–4]. In contrast, the H150 sample shows a significantly larger plastic strain (up to nearly 6 %). The stress–strain curves of the additional samples tested are consistent with those presented and are shown in the supplementary material, confirming the previous observations.

Insets on the curves allow to get information about the serrated behaviour, as depicted by repeated cycles of rapid stress drops followed by reloading, see Fig. 2 c–e). The H100 material exhibits amplitude serrations of the order of 10 MPa directly after yielding and failure occurs rapidly (Fig. 2 c). In contrast, the H150 sample is only experiencing small serrations of the order of 1–2 MPa within the same strain range. Only close to failure, larger serrations start to appear for the H150 sample.

3.3. Porosity characterization

The pore populations were characterised in more detail thanks to the analysis of the X-ray microtomography images (see Fig. 3). The 3D renderings (2.5 mm in diameter and 6 mm in height) of the porosity content are displayed in Fig. 3 a–b) and show both an increase of the porosity content with the hatch spacing (90 pores mm^{-3} and 350 pores mm^{-3} for H100 and H150, respectively), as well as the absence of pores clusters.

In addition, the histograms of the porosity sizes and edge-to-edge distances between first nearest neighbor pores are displayed in Fig. 3 c–d). With the increase of the hatch value, the average pore size is slightly increased while the edge-to-edge nearest pore distance is reduced by 30 %. It structurally depicts the increase of the overall porosity content throughout the creation of more numerous pores and of similar sizes rather than the appearance of some individual very large pores. This is further illustrated by the standard deviation (SD) values of the edge-to-edge pore distance which is smaller for the H150 sample, suggesting a more spatially defined distribution of pores. As emphasized by the work of Shi et al. [9], the absence of pore clusters is of primary importance. Indeed, the FE modelling of metallic glass under uniaxial tensile loading conducted in their work highlighted that main shear bands potentially leading to failure are more prone to form and propagate in the vicinity of pore clusters.

4. Discussion

Uniaxial compression tests revealed that the more porous sample (H150) achieved a similar yield stress to its denser counterpart (H100), but a larger plastic strain. The absence of a yield stress drop in the H150 sample is attributed to its low porosity level (*i.e.* below 1 %). Further increasing the porosity content may enhance plasticity, but a stress drop is expected to occur for a porosity level of several percent, as obtained by Zhang et al. [13] in $Zr_{60}Cu_{22}Fe_5Al_{10}Ag_3$. The similarity in yield stress

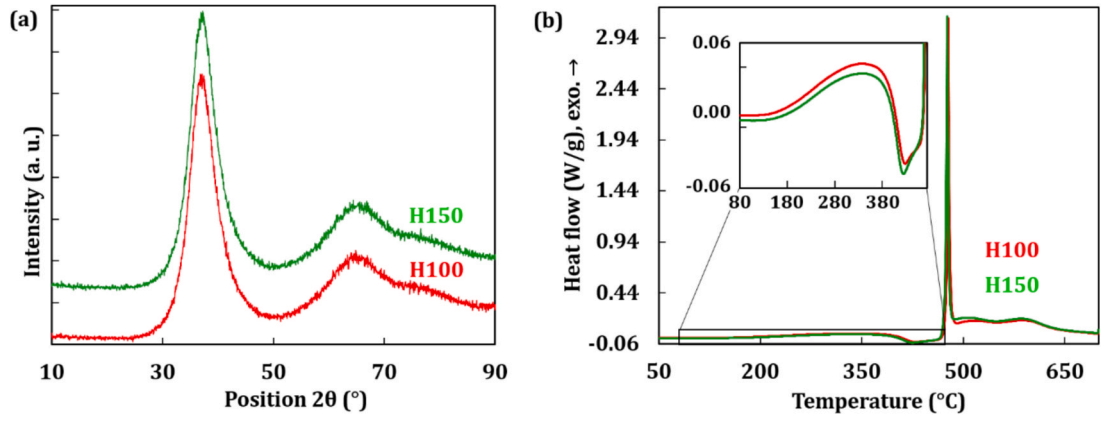

Fig. 1. a) X-ray diffraction patterns of the H100 and H150 $Zr_{59.3}Cu_{28.8}Al_{10.4}Nb_{1.5}$ samples, and b) DSC curves of the H100 and H150 $Zr_{59.3}Cu_{28.8}Al_{10.4}Nb_{1.5}$ samples, including an inset close to T_g.

Table 2
Characteristic thermal properties derived from the DSC analysis of the printed $Zr_{59.3}Cu_{28.8}Al_{10.4}Nb_{1.5}$ specimens, along their oxygen content, porosity level and hardness.

Sample	Tg_o (°C)	Tx_o (°C)	Tp (°C)	ΔTx (°C)	ΔH_{relax} (J/g)	Oxygen (ppm)	Porosity (%)	HV1kgf
H100	393	472	477	79	6,6	964	0.09	478 ± 11
H150	392	473	476	81	5,4	1070	0.75	469 ± 2

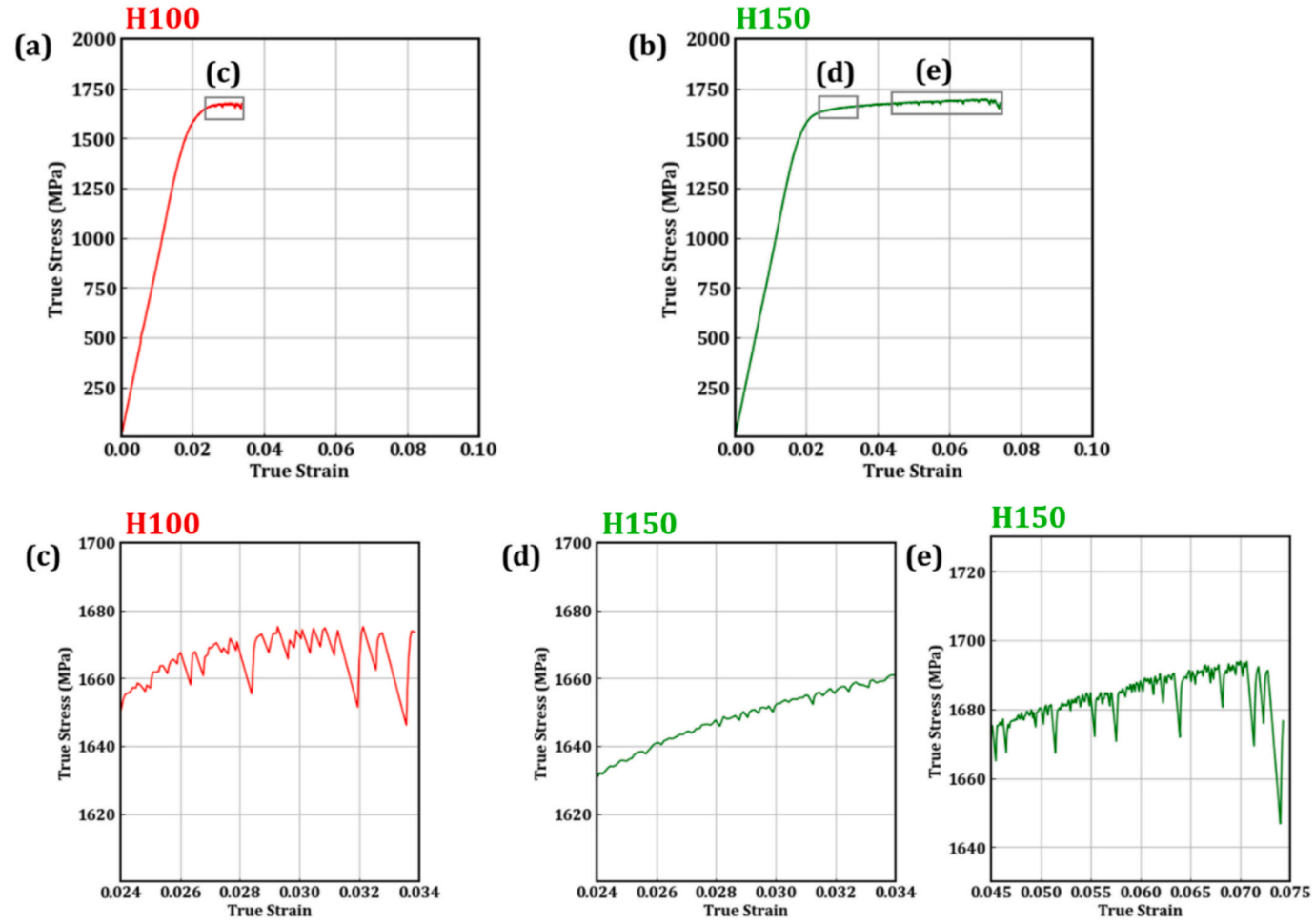

Fig. 2. a) Compression curve of the H100 sample, b) compression curve of the H150 sample, c–e) close-up of the curves extracted in the plastic regimes for better visualisation of the serrated flow.

between H100 and H150 is attributed to their similar structural state, as confirmed by XRD, hardness testing and DSC analysis. Therefore, to our opinion, the difference in plastic strain is connected to the porosities and how they interact with the shear bands. This topic is discussed in more detail in the following section.

4.1. *Interaction pores/shear bands*

Fig. 4 presents observations of the fracture surfaces. Both samples exhibit a similar vein pattern, with varying cell sizes and orientations, see Fig. 4 a–b), similar to what found for the $Zr_{52.5}Cu_{17.9}Ni_{14.6}Al_{10}Ti_5$ investigated by Pauly et al. [24]. Pores are also visible on the fracture surface of the most porous sample as shown in Fig. 4 c–d), alongside liquid features. These are a signature of the temperature rise in the plastic zone during failure and their morphology reveals important viscous flow during their formation. More importantly, regular striations can be observed in the vicinity of the pores, suggesting possible interactions between the pores and shear bands (see yellow arrows). Further interpretation of the fracture surfaces is difficult as they only provide an image of what happened upon failure.

To visualise more clearly the pore-shear band interactions upon deformation, an additional compression test was conducted on a H150 sample of similar height and diameter as previously tested ones, but with a polished facet. The sample was loaded under the same strain rate and serrations were recorded. The test was interrupted and the sample unloaded when 4 % of plastic strain was reached. The polished surface was then observed by SEM, see Fig. 5 a–b). Numerous shear bands are observed, consistent with the measured high ductility under compression. In Fig. 5 a), one can see that shear bands are mostly connecting between two neighbouring pores. This confirms that the pores act significantly on the shear band propagation. In connection to this, the work of Sarac and Schroers [12] on the deformability of porous $Zr_{35}Ti_{30}Cu_{7.5}Be_{27.5}$ metallic glass produced by lithography includes FEM simulation based on a linear elastic material model. The latter highlights that under tensile loading, the complex stress field drives the shear bands towards neighbouring pores [12]. Finally, in the present work, at the scale of a single pore, there is some indication that shear bands also initiate at the pore edges, as shown on Fig. 5(b). In brief, these

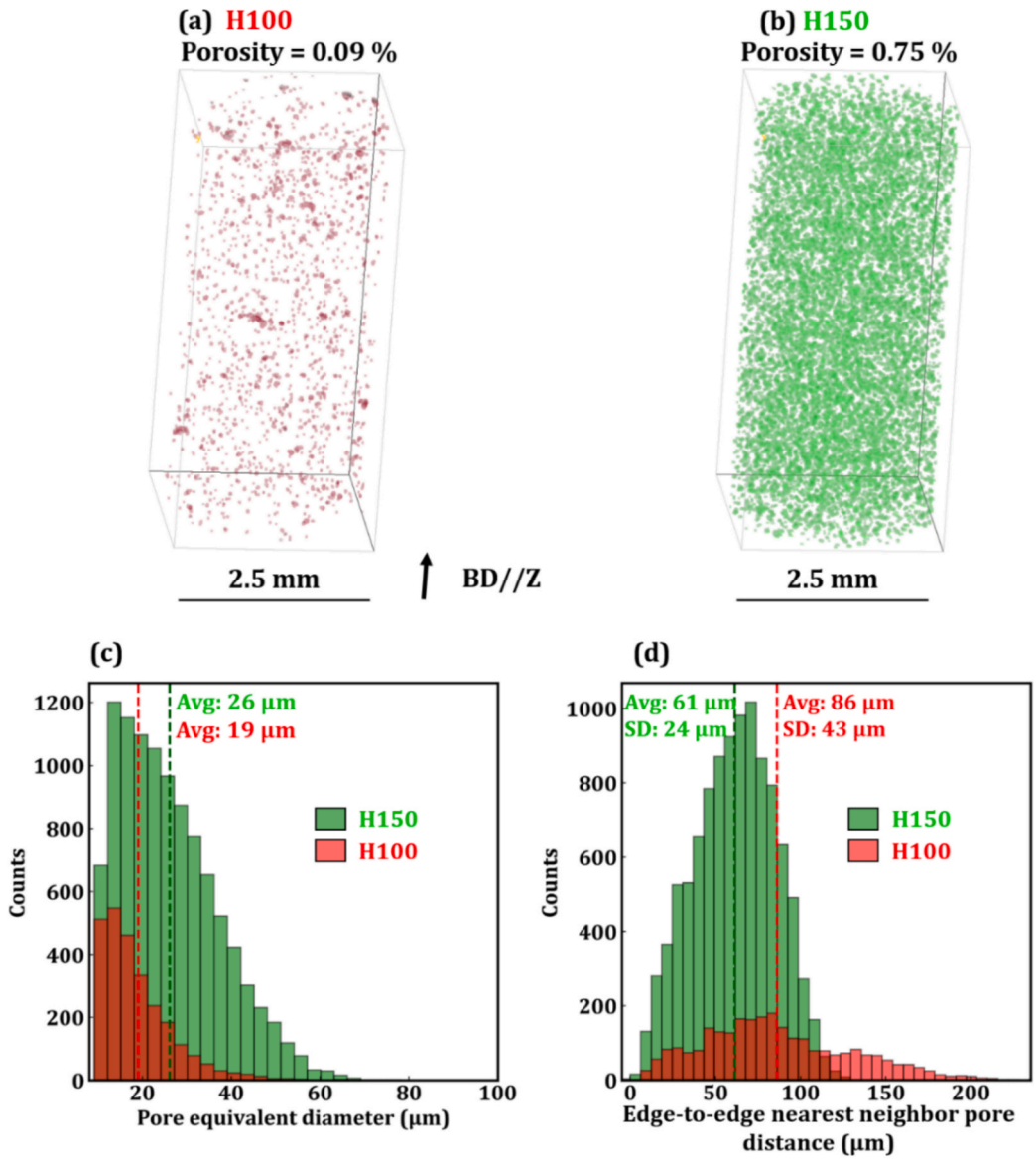

Fig. 3. a–b) The 3D volume renderings of the porosity analysed by XCT in the H100 and H150 samples. c) Distribution of the pore equivalent diameters and d) distribution of edge-to-edge pore distances of nearest neighbours for the H100 and H150 samples. The average values (Avg) are indicated by the dashed lines for the two sample types, the standard deviations (SD) are also noted.

observations suggest that the pores play a trapping role with respect to the shear band, while they contribute to some extent to shear bands nucleation too. As raised in the modelling work of Yang et al. [25], pores may locally alter the heat dissipation, potentially leading to local structural changes in their vicinity. While the conducted material characterization reveals no crystallisation onset nor significant differences in the relaxation state between the H100 and H150 samples, it would be interesting to explore in the future whether such local heterogeneities exist and determine whether they would interact with the shear bands alongside the physical interfaces introduced with the pore.

Modelling work on these interactions between pores and shear bands has shown that the spatial distribution of pores is also key to promoting plasticity [12]. This calls for further analysis of the pore distribution in the H150 sample. To this aim, representative tomography slices in the plane perpendicular to the building-axis are presented in Fig. 6. The spatial distribution of the pores in the H150 sample is clearly not random with pores locally aligned on adjacent dashed lines as drawn on the slices. The angle between two sets of lines is approximately 60 to 67°, with pores present at their intersections. The pattern resulting from these intersecting lines rotates over the sample height, see Supplementary Video. This means that the organisation in the XY plane is directly connected to the 67° rotation of the laser pattern between the layers, with pores present in the interbed regions and connecting through several layers. At a given height, the pattern resulting from the pore organisation is only partially present, as pore nucleation and growth are not identical throughout the layer, depending on the overlap of successive laser beads. Nevertheless, this shows that the distribution of pores is not random and can be controlled by the hatch spacing distance. It is interesting to note that the increase of hatch distance allows increasing the porosity while simultaneously refining the spatial distribution of pores, as seen in Fig. 3. Such a result is not what could be expected for more conventional crystalline alloys processed by LPBF such as 316L stainless steel [26]. This highlights a favourable combination of process parameters, primarily the hatch distance and laser power, with the particular property of the glass which is its high viscosity.

The investigation of the pore distribution in the plane parallel to the building and loading direction has also been performed. Due to the 67°

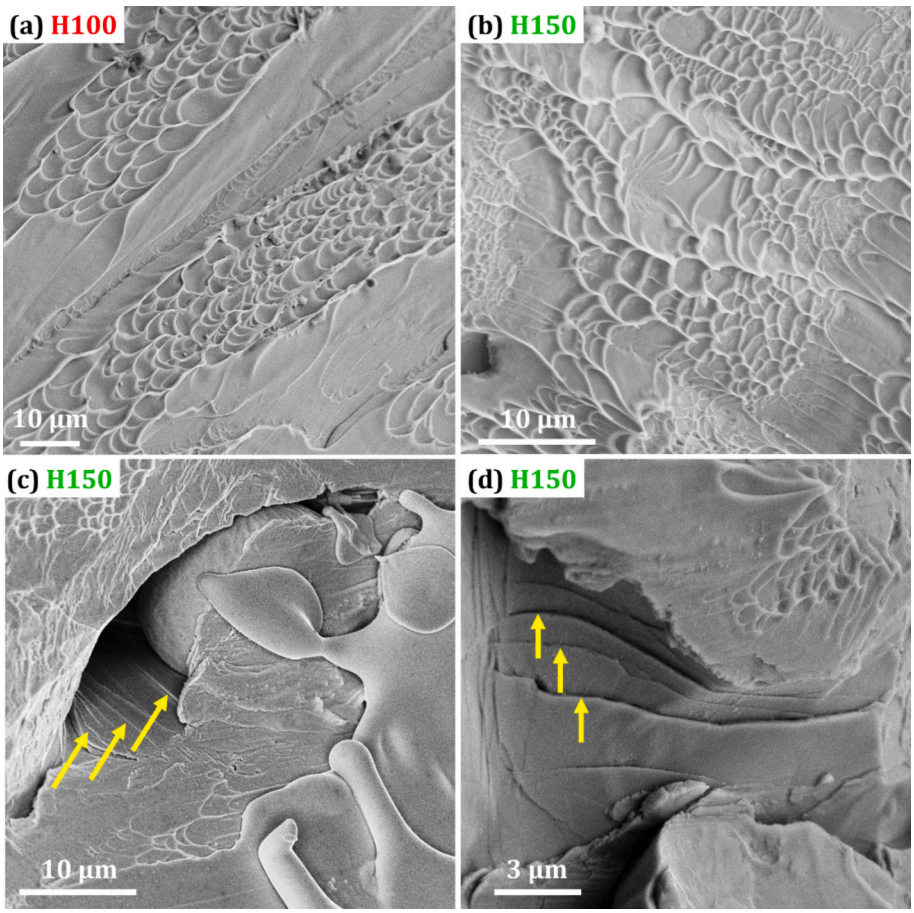

Fig. 4. a–b) Typical fracture surface features of the printed samples with river-like patterns for the H100 and H150 samples; c–d) Apparent pores with step-like features pointed out in yellow for the H150 sample.

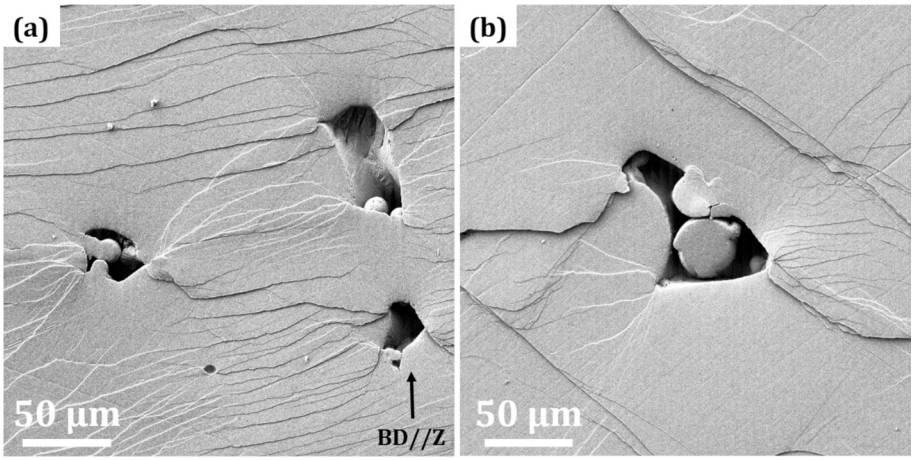

Fig. 5. a–b) SEM micrographs highlighting pore – shear band interactions in the H150 sample.

rotation of the laser between layer, a clear repeatable pattern cannot be observed in this direction. However, several locations can be found into which remarkable layout of pores, as shown in Fig. 7 a), are identified. Such pattern is similar to the one proposed by Zhang et al. [14], reprinted in Fig. 7 b). Zhang et al. simulated the tensile deformation of the Vitreloy1 grade, with a porosity content of 4 %, spatially distributed within different pattern. Their results showed that shear bands propagate preferentially along the directions formed by first and second nearest neighbour pores (illustrated in the present case with dashed-red and dashed-blue lines in Fig. 7 a), respectively). Therefore, they found that the most favourable porosity pattern to promote plasticity is the "AB" pattern composed in 2D of superimposed lines of pores shifted by half the pore-to-pore distance. Remarkably, this is exactly what can be observed in the H150 sample in Fig. 7 a). With this spatial distribution, the lines of first and second nearest neighbours make an angle of around 30° and 60° with the loading axis, respectively. Consequently, this configuration offers the combination of the furthest angles for the two lines of pores compared to the maximum shear stress direction at 45°.

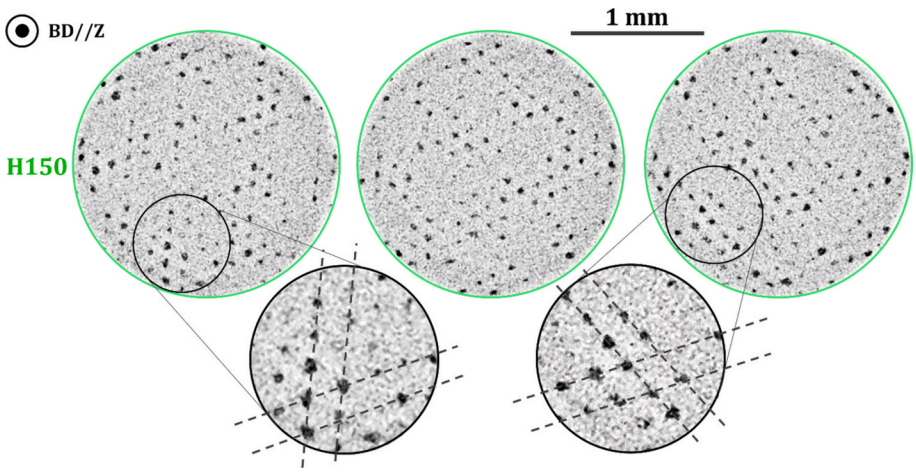

Fig. 6. Three different XCT representative slices extracted at different positions along the building direction and showing the distribution of the pores in planes perpendicular to the building direction (BD) for the H150 sample. Close ups are also displayed to highlight the alignment of pores.

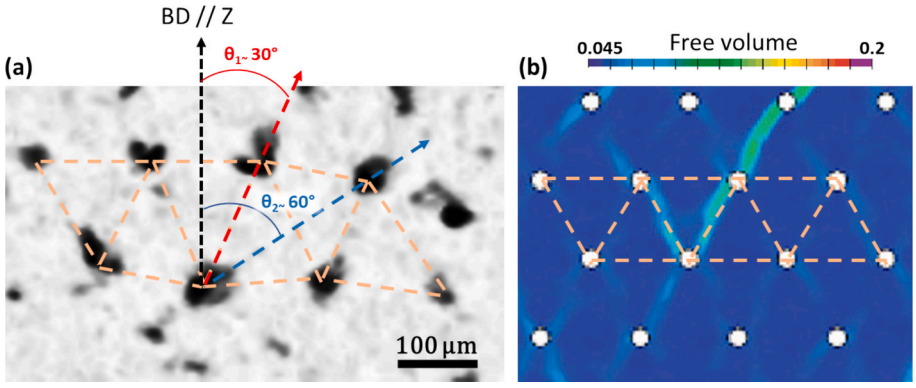

Fig. 7. a) Image extracted from a tomography 2d slice parallel to the loading directions where the pores pattern exhibits similar arrangement than in previous simulated work and which promotes maximum plasticity [14]. b) Porosity pattern (white dots) and free volume content visualisation (colorbar) at 3% of macro-strain of a porous MG with AB pattern (Reprinted and adapted from Publication [14] Copyright (2025), with permission from Elsevier).

Thus, AM achieves several objectives here: achieving a sufficiently low amount of porosity to avoid reduction of yield strength, avoiding pore clusters formation detrimental for plasticity [19], and even more importantly, obtaining a favourable spatial distribution of pores that compel shear bands to propagate along paths distant from the maximum shear stress direction, which enhances plasticity. These findings present an opportunity to enhance the plasticity of AM BMGs through pore control. To fully realise this, future work should explore the interplay between porosity fraction, pore size and distribution with respect to shear band interaction, both through modelling and the production of additional samples with different pore populations.

4.2. Impact on mechanical behaviour

Qualitative interpretation of pore-shear band interaction that correlates with published simulation work has been proposed by post-mortem analysis of the samples. It is however intriguing to see if such interactions can be unravelled by the footprint of the shear band activity during deformation. The serrated flow behaviour in the plastic regime of stress–strain curves can be such a footprint. The serration process is characterized by repeated cycles of a sudden stress drop followed by reloading elastically. The detected stress drops as a function of the compressive strain in the plastic regime are presented in Fig. 8 a–b) for both sample types. The H100 sample displays few serrations of small amplitude together with other serration of larger amplitude (around 20 MPa) in a narrow range of plastic strain (0.025–0.03) leading to failure. Concerning the H150 sample, a group of many small serrations (below 8 MPa) can be recorded with no marked correlation with the plastic strain value. This result suggests a limited propagation of shear bands in the H150 sample. For the other serrations, the amplitude gradually increases with the increasing plastic strain until reaching stress drop values of the order of 20 MPa before final failure. The similar "last" stress drop values in both samples may indicate similar failure mechanisms between the two samples but for different ultimate strain values.

To investigate in more details this assumption, the cumulative probability distributions of the stress drop as a function of the stress drop magnitude are plotted in Fig. 8 c). It corresponds to the percentage of stress drops above a certain value. It implies the collective motion of multiple shear bands [27] and it is well-fitted by a power-law coupled with a square exponential decay function, according to:

$$P(s) = As^{-\beta} exp\left[-\left(\frac{s}{s_c}\right)^2\right] \quad (1)$$

where A is a constant, s is the stress drop, β is the scaling exponent and s_c is the cut-off stress drop. The cut-off stress drop indicates up to which value of the stress drop the power law is still valid. Eq. (1) can fit successfully the data for the H100 sample with fitting values for β and s_c equal to 0.254 and 11 MPa, respectively. These values are similar to those typically reported in the literature for Zr-based metallic glasses [2,9].

For the H150 sample, Eq. (1) can no longer fit the data and two

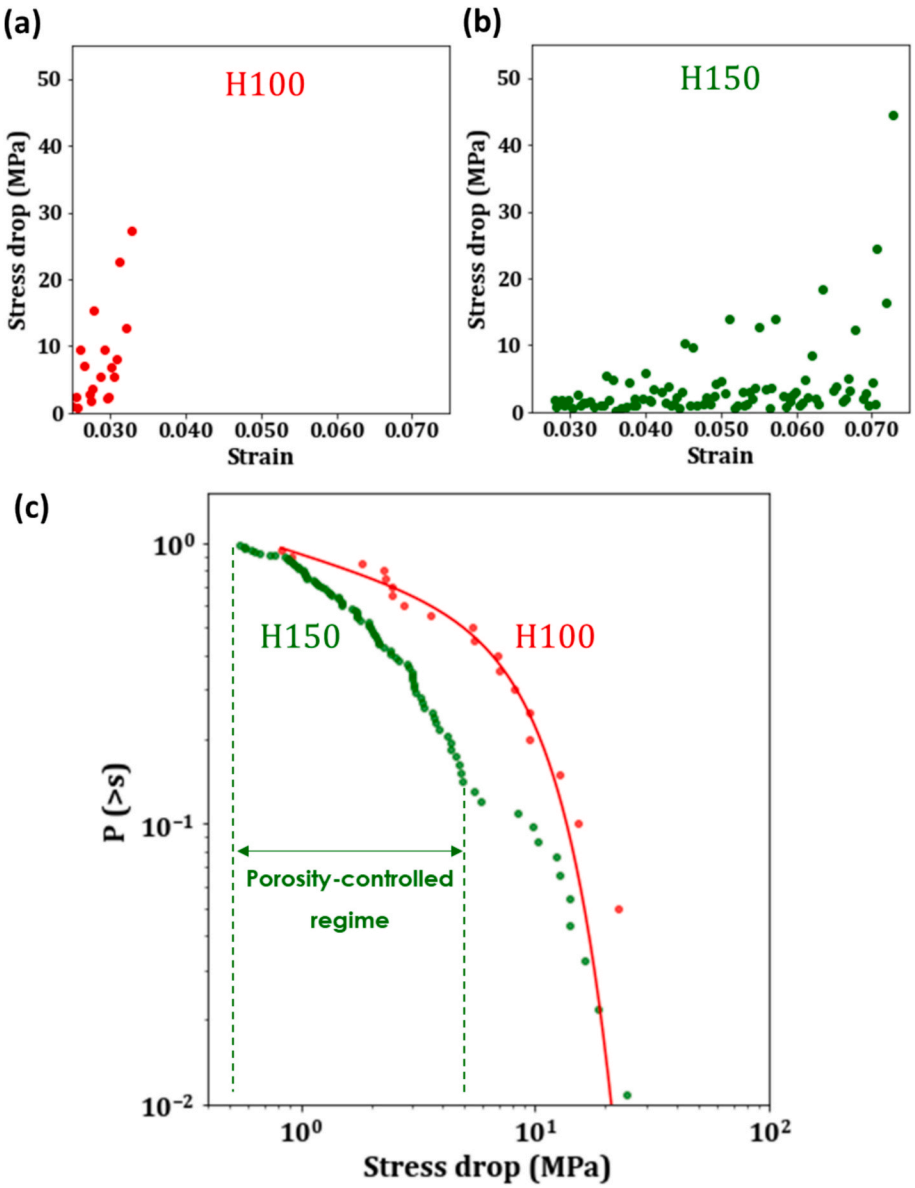

Fig. 8. a–b) Stress drops detected as a function of compressive strain in the H100 sample and H150 sample, respectively. c) Cumulative probability distributions of the stress drop as a function of the stress drop magnitude for the H100 and H150 sample. The corresponding power law fit is displayed for the H100 material.

regimes can be clearly observed. The first one displays many small stress drops, reflecting the enhanced interaction between the pores and the shear bands. This suggests that a large number of shear bands are active and that their propagation is limited, underlining the beneficial role of the pores. The second regime is directly connected to the behaviour observed for the H100 sample. The porosities can no longer limit the propagation of the shear bands, and the fracture behaviour of both the H150 and the H100 samples appears similar. In other words, a transition can be observed between a porosity-controlled regime and a regime that rapidly leads to failure. This confirms that introducing spatially controlled pores is a promising strategy for promoting plasticity and delay failure in additively manufactured metallic glasses.

5. Conclusions

Despite their relatively good processability, Zr-based metallic glasses produced by LPBF generally lack any visible plastic ductility. This study demonstrates that the introduction of a small amount of well-distributed porosities can significantly promote the plasticity of metallic glasses produced by LPBF under compression. It is found that a favourable and non-random distribution of pores can be produced by adjusting the hatch spacing, as pores form preferentially at the interbed regions, due to the hatch spacing effect. This effect enables predictable pore placement. The resulting structure promotes porosity/shear band interaction. An analysis of the pore population using X-ray microtomography revealed that the pores are aligned away from the direction of maximum shear stress. Statistical analysis of the serrated flow of the porous sample reveals a porosity-controlled regime in which small stress drops delay catastrophic failure of the sample. Finally, due to the low volume fraction of porosity, the porous metallic glass retains high strength. The presented results pave the way for the production of strong, ductile glass heterostructures using AM. And the findings present several design opportunities for metallic glass components. The hatch spacing can be exploited to primarily control porosity and in turn engineer ductility while maintaining strength. This also opens opportunities for designing functionally graded metallic glass components where ductility could be enhanced in specific critical regions where for example stress concentration might occur. In addition, the design and placement of the BMG

component in the AM build volume with respect to the build direction can be tailored to orient favourably the pore population with respect to the expected loading in service of the component. To summarize, the presented work establishes that pores should be considered as more than mere defects in additively manufactured BMGs and that instead these can be reframed as a design tool.

CRediT authorship contribution statement

Camille Pauzon: Writing – original draft, Visualization, Investigation, Funding acquisition, Formal analysis, Data curation, Conceptualization. **Rémi Daudin:** Writing – review & editing, Visualization, Validation, Methodology, Investigation, Formal analysis, Conceptualization. **Muhammad Fakhry Hatta:** Investigation. **Pierre Lhuissier:** Methodology, Investigation, Data curation. **Jean-Jacques Blandin:** Writing – review & editing, Project administration, Methodology, Funding acquisition, Conceptualization.

Declaration of competing interest

The authors declare that they have no known competing financial interests or personal relationships that could have appeared to influence the work reported in this paper.

Acknowledgments

Funded by the European Union under the grant agreement “ROSAMA2” n°101059435 (MSCA-PF). Views and opinions expressed are however those of the author(s) only and do not necessarily reflect those of the European Union or REA. Neither the European Union nor the granting authority can be held responsible for them. This work also benefited from the investments made by the Center of Excellence of Multifunctional Architectured Materials “CEMAM” n°AN-10-LABX-44-01, and from the facilities available on the characterization platform CMTC of Grenoble INP-UGA.

Appendix A. Supplementary data

Supplementary data to this article can be found online at https://doi.org/10.1016/j.matdes.2025.115145.

Data availability

Data will be made available on request.

References

[1] N. Sohrabi, J. Jhabvala, G. Kurtuldu, M. Stoica, A. Parrilli, S. Berns, E. Polatidis, S. Van Petegem, S. Hugon, A. Neels, J.F. Löffler, R.E. Logé, Characterization, mechanical properties and dimensional accuracy of a Zr-based bulk metallic glass manufactured via laser powder-bed fusion, Mater. Des. 199 (2021) 1–14, https://doi.org/10.1016/j.matdes.2020.109400.

[2] L. Deng, K. Kosiba, R. Limbach, L. Wondraczek, U. Kühn, S. Pauly, Plastic deformation of a Zr-based bulk metallic glass fabricated by selective laser melting, J. Mater. Sci. Technol. 60 (2021) 139–146, https://doi.org/10.1016/j.jmst.2020.06.007.

[3] Z. Tan, X. Jiang, Z. Xi, Z. Zhou, B. Wang, G. Li, D. He, Fabrication of Zr-based bulk metallic glass lattice structure with high specific strength by laser powder bed fusion, Addit. Manuf. 95 (2024) 1–14, https://doi.org/10.1016/j.addma.2024.104556.

[4] B. Li, V. Yakubov, K. Nomoto, S.P. Ringer, B. Gludovatz, X. Li, J.J. Kruzic, Superior mechanical properties of a Zr-based bulk metallic glass via laser powder bed fusion process control, Acta Mater. 266 (2024) 1–16, https://doi.org/10.1016/j.actamat.2024.119685.

[5] N. Sohrabi, M. Hamidi-Nasab, B. Rouxel, J. Jhabvala, A. Parrilli, M. Vedani, R. E. Logé, Fatigue performance of an additively manufactured Zr-based bulk metallic glass and the effect of post-processing, Metals (basel) 11 (2021) 1–19, https://doi.org/10.3390/met11071064.

[6] P. Bordeenithikasem, M. Stolpe, A. Elsen, D.C. Hofmann, Glass forming ability, flexural strength, and wear properties of additively manufactured Zr-based bulk metallic glasses produced through laser powder bed fusion, Addit. Manuf. 21 (2018) 312–317, https://doi.org/10.1016/j.addma.2018.03.023.

[7] D. Ouyang, N. Li, W. Xing, J. Zhang, L. Liu, 3D printing of crack-free high strength Zr-based bulk metallic glass composite by selective laser melting, Intermetallics (barking) 90 (2017) 128–134, https://doi.org/10.1016/j.intermet.2017.07.010.

[8] J.P. Best, J. Ast, B. Li, M. Stolpe, R. Busch, F. Yang, X. Li, J. Michler, J.J. Kruzic, Relating fracture toughness to micro-pillar compression response for a laser powder bed additive manufactured bulk metallic glass, Mater. Sci. Eng. A 770 (2020) 1–8, https://doi.org/10.1016/j.msea.2019.138535.

[9] J. Shi, S. Ma, S. Wei, J.P. Best, M. Stolpe, B. Markert, Connecting structural defects to tensile failure in a 3D-printed fully-amorphous bulk metallic glass, Mater. Sci. Eng. A 813 (2021) 1–15, https://doi.org/10.1016/j.msea.2021.141106.

[10] N. Sohrabi, A. Parrilli, J. Jhabvala, A. Neels, R.E. Logé, Tensile and impact toughness properties of a Zr-based bulk metallic glass fabricated via laser powder-bed fusion, Materials 14 (2021) 1–15, https://doi.org/10.3390/ma14195627.

[11] T. Wada, A. Inoue, A.L. Greer, Enhancement of room-temperature plasticity in a bulk metallic glass by finely dispersed porosity, Appl. Phys. Lett. 86 (2005) 1–3, https://doi.org/10.1063/1.1953884.

[12] B. Sarac, J. Schroers, Designing tensile ductility in metallic glasses, Nat. Commun. 4 (2013) 1–7, https://doi.org/10.1038/ncomms3158.

[13] P. Zhang, C. Zhang, L. Liu, Toughening 3D-printed Zr-based bulk metallic glass via synergistic defects engineering, Mater. Res. Lett. 10 (2022) 377–384, https://doi.org/10.1080/21663831.2022.2054291.

[14] X. Zhang, S. Zuo, F. Yang, Q. Wang, Y. Sun, Enhancing tensile ductility of porous metallic glasses through shear band path design, J. Non Cryst. Solids 620 (2023) 1–8, https://doi.org/10.1016/j.jnoncrysol.2023.122601.

[15] L. Deng, A. Gebert, L. Zhang, H.Y. Chen, D.D. Gu, U. Kühn, M. Zimmermann, K. Kosiba, S. Pauly, Mechanical performance and corrosion behaviour of Zr-based bulk metallic glass produced by selective laser melting, Mater. Des. 189 (2020), https://doi.org/10.1016/j.matdes.2020.108532.

[16] J.J. Marattukalam, V. Pacheco, D. Karlsson, L. Riekehr, J. Lindwall, F. Forsberg, U. Jansson, M. Sahlberg, B. Hjörvarsson, Development of process parameters for selective laser melting of a Zr-based bulk metallic glass, Addit. Manuf. 33 (2020) 1–8, https://doi.org/10.1016/j.addma.2020.101124.

[17] X. Li, Y. Liu, C. Tan, Y. Zou, Porosity formation mechanisms, microstructure evolution and mechanical performance of AlMgScZr alloy fabricated by laser powder bed fusion: effect of hatch distance, J. Manuf. Process. 94 (2023) 107–119, https://doi.org/10.1016/j.jmapro.2023.03.047.

[18] National Institutes of Health, ImageJ: Image Processing and Analysis in Java, (n. d.). https://imagej.net/ij/index.html (accessed May 15, 2025).

[19] V. Boulos, L. Salvo, V. Fristot, P. Lhuissier, D. Houzet, Investigating Performance Variations of an Optimized GPU-Ported Granulometry Algorithm, Rhodes Island, Greece, 2012.

[20] J.L. Bentley, Multidimensional binary search trees used for associative searching, Commun. ACM 18 (1975) 1–9.

[21] C. Pauzon, A. Raza, E. Hryha, P. Forêt, Oxygen balance during laser powder bed fusion of alloy 718, Mater. Des. 201 (2021) 1–10, https://doi.org/10.1016/j.matdes.2021.109511.

[22] C. Pauzon, K. Dietrich, P. Forêt, S. Dubiez-Le Goff, E. Hryha, G. Witt, Control of residual oxygen of the process atmosphere during laser-powder bed fusion processing of Ti-6Al-4V, Addit. Manuf. 38 (2021) 1–10, https://doi.org/10.1016/j.addma.2020.101765.

[23] C. Pauzon, R. Daudin, P. Lhuissier, X. Bataillon, P. Lapouge, P. Hébrard, P. Peyre, F. Coste, L. Varoto, E. Boller, J.J. Blandin, In situ porosity imaging during laser rescanning of Zr-based metallic glass by Laser Powder Bed Fusion, Addit. Manuf. Lett. 15 (2025) 1–9, https://doi.org/10.1016/j.addlet.2025.100318.

[24] S. Pauly, C. Schricker, S. Scudino, L. Deng, U. Kühn, Processing a glass-forming Zr-based alloy by selective laser melting, Mater. Des. 135 (2017) 133–141, https://doi.org/10.1016/j.matdes.2017.08.070.

[25] Z. Yang, M. Markl, C. Körner, Comprehensive numerical investigation of laser powder bed fusion process conditions for bulk metallic glasses, Addit. Manuf. 81 (2024), https://doi.org/10.1016/j.addma.2024.104026.

[26] R. Gunnerek, Z. Chen, E. Hryha, Impact of high-productivity process parameters in powder bed fusion–laser beam on microstructure of stainless steel 316L, Eur. J. Mater. 3 (2023) 1–24, https://doi.org/10.1080/26889277.2023.2292987.

[27] C. Wang, B.A. Sun, W.H. Wang, H.Y. Bai, Chaotic state to self-organized critical state transition of serrated flow dynamics during brittle-to-ductile transition in metallic glass, J. Appl. Phys. 119 (2016) 1–5, https://doi.org/10.1063/1.4941320.